nature communications



Article

https://doi.org/10.1038/s41467-024-55517-y

Stabilization of oxygen vacancy ordering and electrochemical-proton-insertion-and-extraction-induced large resistance modulation in strontium iron cobalt oxides Sr(Fe,Co)O_y

Received: 27 June 2024

Accepted: 11 December 2024

Published online: 02 January 2025

Check for updates

Yosuke Isoda ¹, Thanh Ngoc Pham ^{2,3,4} ⋈, Ryotaro Aso ⁵, Shuri Nakamizo⁶, Takuya Majima ⁶, Saburo Hosokawa⁷, Kiyofumi Nitta⁸, Yoshitada Morikawa ^{2,9,10,11}, Yuichi Shimakawa ¹ & Daisuke Kan ¹ ⋈

Electrochemically inserting and extracting hydrogen into and from solids are promising ways to explore materials' phases and properties. However, it is still challenging to identify the structural factors that promote hydrogen insertion and extraction and to develop materials whose functional properties can be largely modulated by inserting and extracting hydrogen through solid-state reactions at room temperature. In this study, guided by theoretical calculations on the energies of oxygen reduction and hydrogen insertion reactions with oxygen-deficient perovskite oxides, we demonstrated that the oxygen vacancy ordering in $Sr(Fe_{1-x}Co_x)O_y$ (SFCO) epitaxial films can be stabilized by increasing the Co content ($x \ge 0.3$) and revealed that it plays a key role in promoting proton accommodation into the SFCO lattice. We also show that the electrical resistance of SFCO films can be reversibly modulated by electrochemical proton insertion and extraction, and the modulation exceeds three orders of magnitude for Sr(Fe_{0.5}Co_{0.5})O_{2.5} epitaxial films. Our results provide guidelines for controlling material properties through the insertion and extraction of hydrogen and for designing and exploring hydrogen-insertion materials.

Hydrogen insertion and extraction are promising methods for exploring and controlling materials' properties¹⁻¹⁷ because hydrogen atoms (and protons) have relatively high mobility in solids, even at room temperature. Recent investigations showed that electrochemical

reduction reactions, for example, those induced by hydrogen spillover^{18–22} and by hydrogen injection^{23–27}, can be utilized to insert hydrogen into transition metal oxides. Furthermore, such hydrogen-inserted oxides undergo phase transformations associated with the

¹Institute for Chemical Research, Kyoto University, Uji, Kyoto, Japan. ²Department of Precision Engineering, Graduate School of Engineering, Osaka University, Suita, Osaka, Japan. ³An Giang University, Long Xuyen, Vietnam. ⁴Vietnam National University, Ho Chi Minh city, Vietnam. ⁵Department of Applied Quantum Physics and Nuclear Engineering, Kyushu University, Fukuoka, Japan. ⁶Department of Nuclear Engineering, Kyoto University, Kyoto, Japan. ⁷Faculty of Materials Science and Engineering, Kyoto Institute of Technology, Kyoto, Japan. ⁸Japan Synchrotron Radiation Research Institute, SPring-8, Sayo, Hyogo, Japan. ⁹Innovative Catalysis Science Division, Institute for Open and Transdisciplinary Research Initiatives (ICS-OTRI), Osaka University, Suita, Osaka, Japan. ¹⁰Research Center for Precision Engineering, Graduate School of Engineering, Osaka University, Suita, Osaka, Japan. ¹¹Nanotechnology Program, Faculty of Advanced Technology and Engineering, Vietnam Japan University, Vietnam National University, Hanoi, Luu Huu Phuoc, Nam Tu Liem, Hanoi, Viet Nam. e-mail: thanh@cp.prec.eng.osaka-u.ac.jp; dkan@scl.kyoto-u.ac.jp

emergence of novel physical properties through electron donation from the hydrogen atoms. However, it remains elusive as to which structural factors of materials enable hydrogen insertion and extraction and enhance their effect. Moreover, it is still a challenge to develop materials whose physical properties can be modulated by inserting and extracting hydrogen via solid-state reactions at room temperature.

Electrochemical redox reactions in transistor structures with gate layers of electrolytes containing protons and water molecules have been shown to be utilized for inserting and extracting hydrogen into and from solids like transition-metal oxides in a reversible and non-volatile manner at room temperature 12,14,15. We previously showed that the perovskite strontium iron oxide SrFeO_{2.8}²⁸ (SFO) film channels whose oxygen vacancies (Vos) are randomly distributed undergo structural and resistance changes in response to electrochemical injection and removal of hydrogen from the Nafion/SFO interface in transistor structures with gate layers of proton-conducting solid electrolytes (Nafion)12,14. However, the amount of hydrogen that could be accumulated in the SFO films was limited to only ~ 0.1 per SFO formula unit cell, implying that electrochemical hydrogen injection forms Vos and that not much hydrogen accumulates in the SFO lattice. It is also worth pointing out that among oxides with perovskite-derived crystal structures, some oxygen-deficient oxides with ordered arrangements of Vos, for example, SrCoO_{2.5}9,11, BalnO_{2.5}23, and GdBaCo₂O_{5.5}29 can accommodate high concentrations of protons, suggesting that Vo ordering plays a role in hindering V_O formation upon hydrogen injection and promoting hydrogen accommodation in oxide lattices. An important implication is that controlling the arrangements of V_Os is key to developing oxides that can accommodate hydrogen and exploring properties resulting from hydrogen insertion and extraction.

In this study, guided by density functional theory (DFT) calculations on the energies of oxygen reduction and hydrogen insertion reactions with oxygen-deficient strontium ferrite $SrFeO_y$ and strontium cobaltite $SrCoO_y$, we show that the oxygen vacancy ordering in $Sr(Fe_{1-x}Co_x)O_y$ (SFCO) epitaxial films, characteristic of the brownmillerite structure, can be stabilized by increasing the Co content ($x \ge 0.3$) and that it promotes proton accommodation into the SFCO lattice. We also show that electrochemical proton insertion and extraction can modulate the electrical resistance of SFCO and that the modulation exceeds three orders of magnitude for $Sr(Fe_{0.5}Co_{0.5})O_{2.5}$ epitaxial films.

Results and discussion

To get insight into the preference between V_O formation and hydrogenation of oxides upon H insertion, we chose oxygen-deficient strontium ferrite $SrFeO_y$ and strontium cobaltite $SrCoO_y$ ($2.5 \le y \le 3$) as model materials (Crystal structures of SrMOy (M = Fe and Co) in the Supplementary Information). To elucidate the V_O formation in $SrMO_y$ (M = Fe and Co) upon H insertion, the oxygen reduction energy ($E_{\rm red}$) is evaluated as the reaction energy of the following reaction

$$SrMO_{\nu} + \delta H_2 \rightarrow SrMO_{\nu - \delta} + \delta H_2O \tag{1}$$

The reduction energy per H₂ is then calculated as

$$E_{\text{red}} = \frac{1}{\delta} \left[E \left(\text{SrMO}_{y-\delta} \right) + \delta E \left(\text{H}_2 \text{O} \right) - E \left(\text{SrMO}_y \right) - \delta E \left(\text{H}_2 \right) \right]$$
 (2)

where $E(SrMO_y)$, $E(H_2O)$, and $E(H_2)$ are the total energies per formula unit of $SrMO_y$, isolated H_2O , and isolated H_2 , respectively. Note that δ is 0.125, whereas we employed $\delta = 0.25$ to evaluate the reduction of $SrMO_{2.75}$ to $SrMO_{2.5}$.

On the other hand, the hydrogen insertion energy needed for $SrMO_y$ (E_H) to become hydrogenated phases ($H_{0.06}SrMO_{2.5}$, $H_{0.06}SrMO_{2.875}$) per H_2 is defined as

$$E_{\rm H} = \frac{1}{0.03} \left[E \left(H_{0.06} SrMO_y \right) - E \left(SrMO_y \right) - 0.03 E \left(H_2 \right) \right]$$
 (3)

Here, $E(H_{0.06} {\rm SrMO}_y)$ is the energy per formula unit of the hydrogenated phase of ${\rm SrMO}_y$. We modeled ${\rm H}_{0.06} {\rm SrMO}_y$ (y = 2.5, 2.75, and 2.875) by adding a single H atom to the ${\rm SrMO}_y$ supercell (Hydrogenation of ${\rm SrMO}_y$ (M = Fe and Co) in the Supplementary Information). The H insertion amount of 0.06 per the ${\rm SrMO}_y$ formula unit (${\rm H}_{0.06} {\rm SrMO}_y$) was selected because, in the experiment 12.14, the H insertion amount in the ${\rm SrFeO}_y$ film was found to be ~ 0.1 H per the ${\rm SrFeO}_y$ formula unit.

Figure 1 plots E_{red} and E_H of SrMO_{ν} (M = Fe and Co) as a function of oxide oxygen stoichiometry (y). It should be noted that Sr₃M₃O₈ (M = Fe and Co) is considered a crystal structure with $2.5 < y \le 2.7$, but it was found to be stable only for the M = Co case. Therefore, it was not included in Fig. 1. More details of the Sr₃M₃O₈ (M = Fe and Co) structure and its stability are provided in Thermodynamic stability of SrFeO_v and SrCoO_v and Supplementary Fig. S2 in the Supplementary Information. The reduction of SrMO_{ν} (ν > 2.7 and M = Fe and Co) to lower O stoichiometry structures by the formation of Vo is preferable because the E_{red} 's are significantly negative and almost constant. On the other hand, the reduction of brownmillerite SrMO_{2,5} is unlikely. The thermodynamic stability of $SrFeO_{\nu}$ and $SrCoO_{\nu}$ is elucidated by calculating the free energy of Vo formation. (Details of our calculations are shown in Thermodynamic stability of SrFeO_v and SrCoO_v and Supplementary Fig. S2 in the Supplementary Information). We find that SrFeO_{ν} with the perovskite structure (y = 2.75 and 3.00) is stable, while $SrCoO_y$ with the brownmillerite structure (y = 2.50) is stable at T = 300 K and under a wide O_2 pressure between 10^{-10} to ~ 0.2 atm. We can thus conclude that SrCoO_v tends to have the brownmillerite lattice with V_O ordering, while SrFeO_v tends to have the perovskite lattice with Vo disordering at room temperature.

Here, we discuss the energetic preference between the Vo formation ($E_{\rm red}$) and hydrogenated phase formation ($E_{\rm H}$) in SrFeO_y and SrCoO_y upon H insertion. For SrFeO_y with the perovskite structure (y > 2.7), $E_{\rm red} < E_{\rm H}$, indicating that the V_O formation in SrFeO_y is the main reaction upon H injection. At y = 2.5 (SrFeO_{2.5}), $0 < E_{\rm H} < E_{\rm red}$, showing that neither the V_O formation nor the hydrogenated phase formation is preferable. In contrast, for SrCoO_y (y > 2.7), both V_O formation and hydrogenation of SrCoO_y are preferable because $E_{\rm H} < E_{\rm red} < -2$ eV. At y = 2.5 (SrCoO_{2.5}), the hydrogenation of SrCoO_{2.5} becomes the main route upon H insertion because the hydrogenated phase is stable with $E_{\rm H} = -2.91$ eV, while the further reduction of SrCoO_{2.5} is unlikely ($E_{\rm red} = -0.46$ eV). Our DFT calculation results raise the possibility that oxygen vacancy ordering in Sr(Fe_{1-x}Co_x)O_y (SFCO), which would promote hydrogen accumulation in their lattices, can be achieved by adjusting the B-site (Fe and Co) cation composition.

To test our idea, we fabricated SFCO epitaxial thin films with a thickness of ~50 nm on (LaAlO₃)0.3-(SrAl_{0.5}Ta_{0.5}O₃)0.7 (LSAT) (001) single crystal substrates by pulsed laser deposition at a substrate temperature of 700 °C and under oxygen pressure of 100 mTorr. To see how the crystal structures of the SFCO films depend on the B-site cation composition, we carried out cross-sectional high-angle annular dark-field (HAADF) and annular bright-field (ABF) imaging in aberration-corrected scanning transmission electron microscopy (STEM). Figure 2 shows HAADF- and ABF-STEM images of SFO, SFCO (x = 0.5), and SCO films. As expected from the thermodynamic stability calculation in Supplementary Fig. S2 and the fact that our films were grown under relatively high oxygen pressures (~100 mTorr), the SFO films have the perovskite structure, and the Fe-Fe and Sr-Sr distances are homogeneous (Fig. 2b, c), in agreement with previous reports ^{12,14,30}. In addition, we can see additional image contrasts in the ABF image

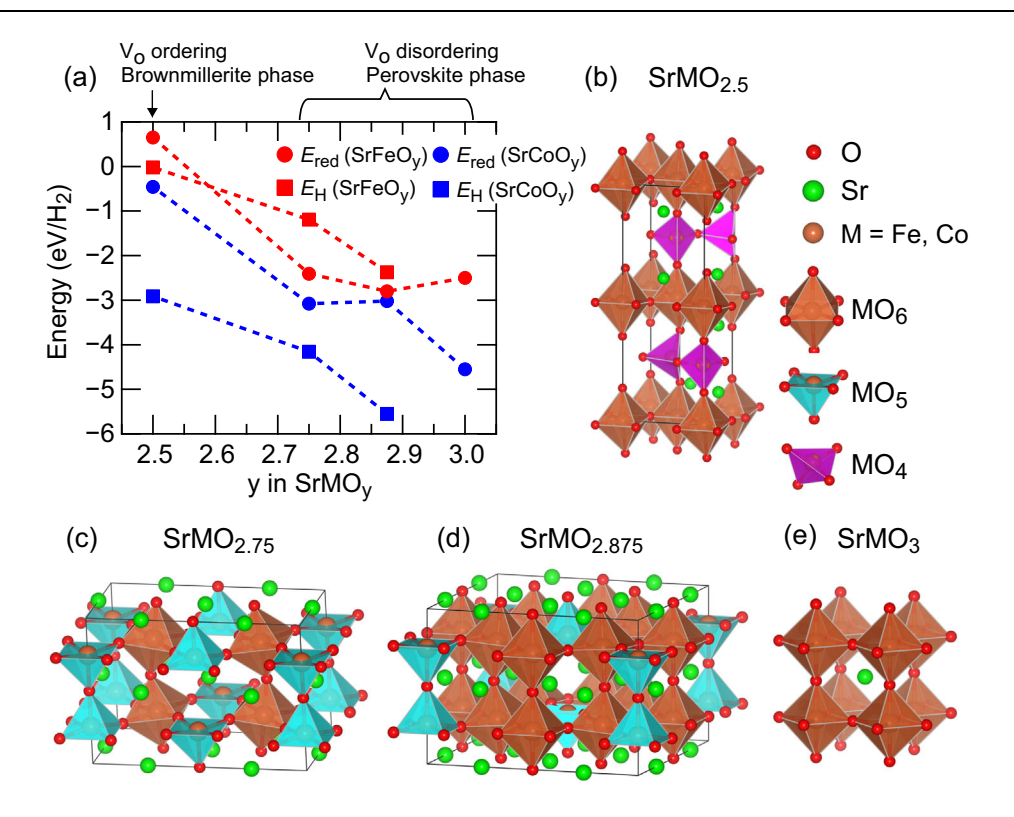


Fig. 1 | **Theoretical investigation of oxygen reduction and protonation of SrFeO_y and SrCoO_y.** a Oxygen reduction energy (E_{red}) and hydrogen insertion energy (E_{H}) of SrMO_y (M = Fe and Co) as a function of oxide oxygen stoichiometry (y). (\mathbf{b} - \mathbf{e}) Crystal structures of SrMO_y were employed to evaluate E_{red} and E_{H} .

corresponding to oxygen atomic columns, whose positions are consistent with those expected from the corner-shared oxygen octahedra in the perovskite structure projected along the [110] direction (Fig. 2c). Our previous ⁵⁷Fe Mössbauer measurements showed that the Fe valence state in perovskite-structured SFO epitaxial films was determined to be + 3.66, and thus, the oxygen content was \sim 2.8²⁸, which also supports that our fabricated SFO film has the perovskite structure with disordered oxygen vacancies (i.e., SrFeO_{2.8}). On the other hand, as can be seen in the HAADF- and ABF-STEM images for the SFCO (x = 0.5) and SCO films (Fig. 2e, f, h, i), Co substitution in SFO films leads to spatial modulation of the atomic distances characteristic of the brownmillerite structure. The out-of-plane distance between the Sr and Fe(Co) atoms is periodically modulated, and oxygen atomic columns undergo concomitant changes associated with the formation of the oxygen vacancy ordering, which is characterized as alternative stacking of the oxygen tetrahedral (Fe,Co)O₄ layers and the octahedral (Fe,Co)O₆ layers along the out-of-plane direction in the SFCO (x = 0.5) and SCO films. The Co-substitution-induced lattice modulations and oxygen vacancy ordering can not be explained by lattice (bond length) modulations without the formation of oxygen vacancies previously observed in perovskite cobaltites³¹. We also performed electron energy-loss spectroscopy (EELS) elementary mapping for the SFCO (x = 0.5) film and confirmed that Fe and Co in the B-site in the x = 0.5film are disordered (Supplementary Fig. S7).

The perovskite-to-brownmillerite structural transformation induced by substituting Fe with Co in SFCO films can be further confirmed by X-ray diffraction measurements. Figure 3a shows the $2\theta/\theta$ diffraction patterns for as-grown SFCO films with x = 0, 0.3, 0.5, 0.7, and 1.0. Regardless of the fraction of Co substitution, all films exhibit the fundamental (0 0 2) $_{pc}$ reflection (pc denotes the pseudo-cubic perovskite notation), thus confirming the epitaxial growth of SFCO layers on the substrates. In addition, as shown in Fig. 3b, where the (0 0 3/2) $_{pc}$ superstructure intensity is plotted against the Co concentration, the superstructure peaks begin to appear at 30% Co substitution and

develop with further increasing Co substitution. It should be noted that superstructure peaks resulting from the oxygen vacancy ordering are observed only along the out-of-plane direction, not along the inplane direction (Supplementary Fig. S5), indicating that the oxygen vacancy ordering in the SFCO films grown on LSAT substrates forms along the out-of-plane direction. Figure 3c shows the Co-substitution dependence of the out-of-plane and in-plane lattice constants of the SFCO films. The out-of-plane constant was determined from the (002)_{pc} reflection position, while the in-plane constants were determined from positions of the (114)_{pc} SFCO reflection in the reciprocal space mappings around the (2 2 8) LSAT reflections (Supplementary Fig. S4). The out-of-plane lattice constant $c_{\rm pc}$ (based on the pseudocubic perovskite notation) is ~3.88 Å for the as-grown SFO films, whereas it slightly increases with the Co substitution up to 50%, and it jumps to 3.96 Å at the 70% Co substitution. The in-plane lattice constants in Fig. 3c also indicate that the SFCO films with Co substitution up to 50% maintain the tetragonal structure whose in-plane lattices are fixed by the substrate lattices. With further Co substitution, the inplane lattice constants $a_{\rm pc}$ and $b_{\rm pc}$ of the SFCO films with $x \ge 0.7$ become different from each other, as confirmed by the observation of the (1 0 16) and (0 1 16) reflections (in the orthorhombic perovskite notation) seen at different reciprocal space positions. (Supplementary Fig. S4). Given that the brownmillerite structure of the bulk SrCoO_{2.5} has orthorhombic symmetry, our STEM and X-ray diffraction characterizations indicate that increasing the Co composition in SFCO films reduces the oxygen content from 2.8 to 2.5, leading to structural transformation from the perovskite structure with disordered oxygen vacancies (x < 0.3) to the brownmillerite structure with ordered oxygen vacancies ($x \ge 0.3$). These observations are in good agreement with the theoretical calculation results (Supplementary Fig. S2), where the $SrFeO_{\nu}$ and $SrCoO_{\nu}$ are, respectively, predicted to be stable in the perovskite ($y \ge 2.75$) and brownmillerite crystal structures (y = 2.5) at T = 300 K and under a wide range of O_2 pressure between 10⁻¹⁰ and ~0.2 atm. The Co-substitution-induced reduction in the

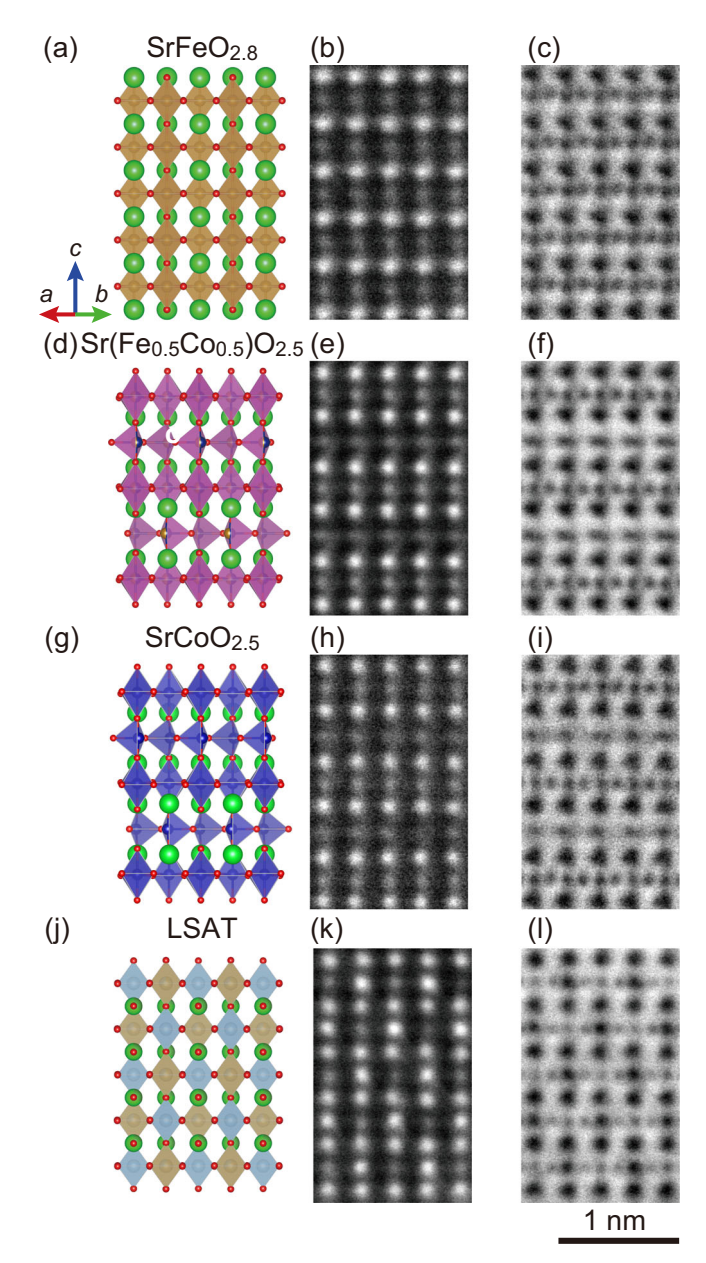


Fig. 2 | **STEM characterization of as-grown SFCO films.** Crystal structures (\mathbf{a} , \mathbf{d} , \mathbf{g} , \mathbf{j}), cross-sectional HAADF- (\mathbf{b} , \mathbf{e} , \mathbf{h} , \mathbf{k}), and ABF-STEM images (\mathbf{c} , \mathbf{f} , \mathbf{i} , \mathbf{l}) for asgrown Sr(Fe_{1-x}Co_x)O_y films with x=0 (\mathbf{a} , \mathbf{b} , \mathbf{c}), x=0.5 (\mathbf{d} , \mathbf{e} , \mathbf{f}), x=1.0 (\mathbf{g} , \mathbf{h} , \mathbf{i}), and LSAT substrates. The STEM images were taken along the [110] direction of LSAT substrates. The crystal structure models were drawn using the VESTA program⁴³. In (\mathbf{a} , \mathbf{d} , and \mathbf{g}), the green and red balls indicate Sr and O atoms, and the balls in oxygen octahedra and tetrahedra correspond to either Fe or Co. In (\mathbf{j}), the green, light blue, beige, and red balls correspond to La/Sr, Al, Ta, and O atoms.

oxygen content and resultant changes in the hybridization between Fe/Co 3 d and O 2p states are also inferred from O-K edge X-ray absorption spectroscopy for the as-grown SFCO films with x = 0, 0.5, and 1.0 (Supplementary Fig. S9).

To see how Co-substitution-induced structural changes affect proton accumulation in SFCO films, we fabricated electric-field-effect transistor structures with channels of SFCO thin films and gate layers of proton-conducting electrolyte (Nafion membranes) and electrochemically injected protons into the SFCO channels by applying gate voltages ($V_{\rm GS}$). X-ray $2\theta/\theta$ diffraction patterns for SFCO films after applying $V_{\rm GS}$ of + 3.5 V for 30 min are shown in Fig. 3a. Compared with the diffraction patterns for as-grown SFCO films, the electrochemical

proton injections are found to result in an additional diffraction peak and a reduction in the intensity of the original SFCO $(002)_{pc}$ reflections whose positions also shifted toward the lower 2θ side. In addition, the $(0\ 0\ 3/2)_{pc}$ superstructures seen for the brownmillerite-structured SFCO films exhibit changes concomitant with the protonation-induced changes in their fundamental $(002)_{pc}$ reflection, indicating that the oxygen vacancy ordering of the brownmillerite lattice is maintained during the protonation process. These results imply that the electrochemically injected protons accumulate into SFCO films' lattices and, as a result, form proton-containing phases of SFCO films.

To further corroborate the protonation of SFCO films, we performed elastic recoil detection analysis (ERDA) at the 1.7 MV tandem accelerator facility of the Quantum Science and Engineering Center, Kyoto University. To quantitatively determine the proton concentration accumulated in the films, the ERDA spectra were simulated and fitted by using the SIMNRA 7.03 software³². The typical ERDA spectra for the films used for X-ray diffraction characterization and their fitting results are shown in Supplementary Fig. S6. Figure 3d shows the Co concentration dependence of the hydrogen concentration in SFCO films protonated by applying $V_{GS} = 3.5 \text{ V}$ for 30 min. Although the protonation in this study was achieved by voltage application through the solid-state electrolyte Nafion membranes, in contrast to previous studies9,11 that often utilized liquid electrolytes such as ionic liquids, the H concentration of the SCO film reaches as large as 1.5 in our protonation condition, indicating that the types of electrolyte do not matter for the protonation. This H concentration is much larger than that expected from the Co valence change from 3 + for SrCoO_{2.5} to 2 + for the protonated film. A recent investigation showed that neutral H-H dimers could be stored in oxygen vacancy channels in the CoO₄ layers of SCO, allowing proton accumulation up to the H concentration of ~ 2 per the formula unit of SCO. The H concentration accumulated in our protonation condition is fairly close to the maximum H concentration and should be large enough to see how Co-substitutioninduced structural changes affect proton accumulation in SFCO films. For the perovskite structured films (x < 0.3) whose oxygen content decreases from 2.8 with the Co substitution, the H concentration remains below ~0.3. On the other hand, for the brownmilleritestructured films ($x \ge 0.3$) whose oxygen content is 2.5, the H concentration increases with the Co substitution. These observations are consistent with the results of the theoretical calculation in Fig. 1, highlighting that the oxygen vacancy ordering prohibits the formation of oxygen vacancies upon electrochemical proton injections and promotes hydrogen accumulation in the SFCO lattices. The lattice expansion associated with H injection to the SFO film with disordered oxygen vacancies is thus understood as a result of oxygen vacancy formation. Given that a small amount of hydrogen is also accumulated in the SFO lattice, the H injection transforms the SFO film to H_{0.1}SrFeO_{2.8-δ} (whose oxygen content probably is close to 2.5). It should be pointed out that in contrast to the SrCoO_{2.5} (SCO) films, only a negligibly small amount of hydrogen is accumulated into the brownmillerite-structured SrFeO_{2.5} films with our protonation condition (Supplementary Fig. S10), which agrees with the previous report¹⁶. An important implication is that in addition to the oxygen vacancy ordering, some other factors should also contribute to the H accumulation in SrCoO_{2.5}, for example, changes in structural energy associated with the protonation-induced lattice expansions and electronic energy associated with electron transfer from hydrogen. Further theoretical investigations will be needed to fully identify factors that allow SrCoO_{2.5} to accumulate large amounts of hydrogen. It might also be worth noting that although the H concentrations of the SFCO films with $x = 0.3 \sim 0.7$ are somehow scattered due to uncertainties associated with the fitting of ERDA spectra, the H concentration of the x = 0.5 SFCO film is slightly higher than that of the x = 0.7 films. This might be related to the fact that the x = 0.5 film has a tetragonal structure, and its brownmillerite orthorhombic distortion

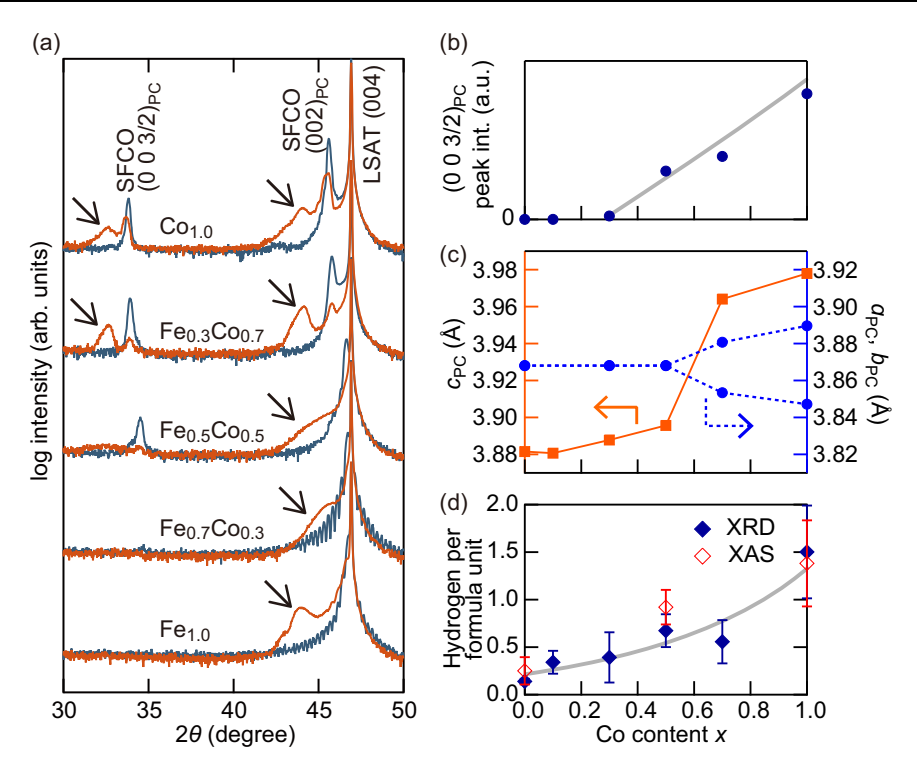


Fig. 3 | **Protonation of SFCO films. a** X-ray $2\theta/\theta$ diffraction patterns for as-grown (blue lines) and protonated SFCO films (orange lines). The films were protonated by applying a gate voltage $V_{\rm GS}$ of 3.5 V for 30 min in transistor structures. The reflections indicated with the arrows originate from the protonated phase of SFCO films. **b-d** Co-substitution-changes in **(b)** the intensity of the $(0\ 0\ 3/2)_{\rm pc}$ superlattice peaks for as-grown SFCO films, **(c)** the out-of-plane and in-plane lattice constants for as-grown SFCO films, and **(d)** hydrogen concentration for protonated SFCO films. The in-plane lattice constants were determined from the $(114)_{\rm pc}$ reflection

positions in reciprocal space mapping measurements (Supplementary Fig. S4). The lattice constants are plotted on the basis of the pseudo-cubic perovskite notation. The hydrogen concentrations of the SFCO films used for the XRD (Fig. 3a) and XAS characterizations (Fig. 4) were obtained from ERDA measurements and plotted with the blue and red symbols, respectively. Error bars in Fig. 3d correspond to the uncertainty in the hydrogen concentration calculated by fitting ERDA spectra. The gray lines in (**b**, **d**) are guides for the eye.

suppressed compared to the x = 0.7 film (Fig. 3c) because such structural modification would affect the energy necessary for proton migration and diffusion through the CoO_4 tetrahedral and CoO_6 octahedral layers.

To evaluate how the proton accumulation affects the electronic structure of SFCO films, we carried out synchrotron X-ray absorption spectroscopy (XAS) for as-grown, protonated, and de-protonated SFCO films (x = 0, 0.5, and 1.0) at the BL01B1 beamline in SPring-8. The protonated SFCO films were prepared by applying $V_{GS} = 3.5 \text{ V}$ for 30 min, and the de-protonated films were prepared by extracting protons from protonated films by applying $V_{GS} = -3.5 \text{ V}$ for 30 min. Figure 4 shows the Fe-K and Co-K edge XAS spectra for the as-grown, protonated, and de-protonated SFCO films. The Fe-K edge spectra of the as-grown films with x = 0 and 0.5 are very similar to each other. This observation implies that hybridization results in electron transfer from the O 2p to Fe 3 d states (the formation of O 2p holes), and the Fe valence state of the SFO film should be regarded as +3, not the nominal valence state of +3.6 expected from its chemical formula, as also suggested by their O-K edge XAS (Supplementary Fig. S9)³³. Furthermore, the Fe-K edge XAS spectra for the SFCO films (x = 0 and 0.5) show no changes associated with protonation and deprotonation, implying that the Fe valence states in the SFCO films (x = 0 and 0.5) remain unchanged at + 3 despite changes in the H and O concentrations in the films. On the other hand, the Co-K edges for the SFCO films (x = 0.5, and 1) shift toward the lower and higher energy sides in association with protonation and de-protonation, respectively. These observations imply that the electronic configurations of Fe (Fe³⁺, 3 d⁵) and Co (Co³⁺, 3 d⁶) in the SFCO films correlate to the protonation and de-protonation of the SFCO films. Fe³⁺ (3d⁵) should have the high-spin and half-filled electron configuration, which is stable and would become largely unstable if electrons were accepted from or donated to hydrogen accumulated in SFCO lattices. On the other hand, Co³+ (3d6), which is in the low-spin configuration and has empty orbitals, can accept and donate electrons associated with protonation and de-protonation processes. Therefore, the protonation and de-protonation of the SFCO lattices mainly affect the Co valence states through electron transfer from hydrogen. These results are also consistent with the fact that the concentration of the proton accumulated in the SFCO lattice increases as the Co substitution increases (Fig. 3d).

We also point out that the protonation and de-protonation reaction is not symmetric in SFCO films. The Co-K edge positions of the asgrown SFCO (x = 0.5) and SCO films are similar to each other and between those of the Co^{2.66+}3O₄ and SrCo⁴⁺O₃ references (for more details, see Supplementary Fig. S8 in Supplementary Information). Nonetheless, the Co-K edge position of the protonated SCO film is much closer to that of the Co²⁺O reference, whereas the Co-K edge position of the protonated SFCO film coincides with that of the Co^{2.66+}₃O₄ reference. Furthermore, the Co-K edge spectra of the de-protonated SFCO films (x = 0.5, and 1) are not back to those of their as-grown films. The Co-K edge of the de-protonated SCO film appears at an energy slightly lower than that of the as-grown SCO film, indicating that the de-protonated film is still reduced with the Co valence state lower than that of the as-grown film (Fig. 4c and Supplementary Fig. S8). On the other hand, the Co-K edge of the de-protonated SFCO film is seen at an energy higher than that of the as-grown SCO film and almost coincides with that of the SrCo⁴⁺O₃ reference. Although X-ray absorption K-edge spectra depend on materials' crystal structures and oxygen coordination environment surrounding transition metals and quantifying valence states of Fe and

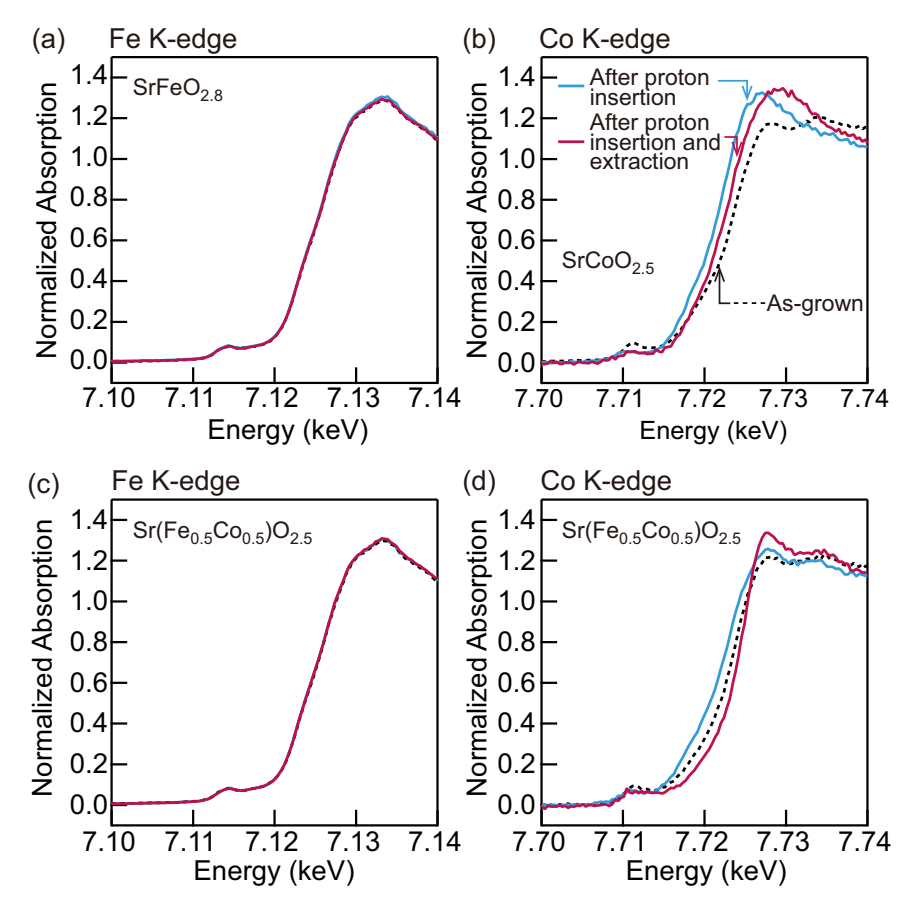


Fig. 4 | **XAS** characterization of protonation and de-protonation of SFCO films. Normalized X-ray absorption near-edge structure spectra in the energy region around (\mathbf{a} , \mathbf{c}) Fe and (\mathbf{b} , \mathbf{d}) Co K-edge absorptions for SFO, SFCO (x = 0.5), and SCO films. For each film, the spectra were obtained in the as-grown, protonated, and deprotonated states. The protonation was carried out by applying a V_G of 3.5 V for

30 min in transistor structures, and the de-protonation was carried out by first applying a $V_{\rm G}$ of 3.5 V for 30 min and subsequently a $V_{\rm G}$ of – 3.5 V for 30 min. The H concentration of the protonated SFO, SFCO (x = 0.5), and SCO films used for the XAS characterization was determined to be – 0.2, – 0.9, and –1.4, respectively, and plotted in Fig. 3d (the red symbols).

Co in the protonated and de-protonated films will need further investigations, our observations indicate that the films with more Co substitutions are more likely to be protonated and less likely to be oxidized (more difficult to extract H from the lattice), which is consistent with the expectation from the H contents accumulated in SFCO films (Fig. 3d). Therefore, the gate voltages and reaction times necessary for inserting H into (unprotonated) SFCO films and extracting H from protonated films are not exactly the same, making the protonation and de-protonation reaction asymmetric.

We also show that electrochemical protonation and de-protonation also modulate the electrical resistance of the SFCO film channels. The results are summarized in Fig. 5. As shown in Fig. 5a, the $V_{\rm GS}$ pulses with durations of 20 s were repeatedly applied to the channels to induce protonation and de-protonation. The total duration of each train of ten consecutive positive (negative) $V_{\rm GS}$ pulses was 200 s. To evaluate the V_{GS} -induced change in the channel resistance R_{DS} by minimizing contributions of leakage currents through the Nafion gate layers, RDS was measured by setting $V_{GS} = 0 \text{ V}$ and $V_{DS} = 0.1 \text{ V}$ after V_{GS} -induced (de-) protonation for 20 s. Figure 5b shows V_{GS} -induced changes in R_{DS} for SrFeO_{2.8}²⁸, Sr(Fe_{0.5}Co_{0.5})O_{2.5}, and SrCoO_{2.5} film channels. We find that regardless of the Co concentration, applying positive and negative V_{GS} increases and decreases the channel resistance, respectively. Given that the channel resistance is measured under the $V_{GS} = 0 \text{ V}$ condition, the observed resistance changes are non-volatile, indicating that V_{GS} induced protonation and de-protonation lead to the resistance changes in the SFCO films. Interestingly, the magnitude of the V_{GS} -induced resistance changes, ΔR , which is defined by the ratio of R_{DS} obtained after applying the last pulse of a positive sequence to that of a negative

 $V_{\rm GS}$ sequence ($\Delta R = R_{\rm High}/R_{\rm Low}$, see Fig. 5a), depends on the Co concentration. For the SFO films (x = 0), ΔR is 10–100, and less V_{GS} -dependent. Given that the hydrogen concentration in the SFO film lattice is small and oxygen vacancies are also created upon H⁺ injection, the effects of the protonation and de-protonation in SFO films are less dominant, while the creation and annihilation of oxygen vacancies, which might be limited to near the surface region, impact on the resistance changes. On the other hand, increasing Co substitution up to x = 0.5 increases ΔR . For the SFCO (x = 0.5) films (Fig. 5b) ΔR is enhanced, and it reaches ~3.0 \times 10³ when $V_{GS} = \pm$ 2.5 V. Note that the oxygen vacancy ordering in SFCO promotes the proton insertion and extraction in the SFCO lattices and the resultant changes in the Co valence state and that the protonation and de-protonation have therefore profound effects on the electrical properties. With further Co substitution, ΔR , however, decreases, as shown by the results for SCO films in the bottom panel of Fig. 5b. Although large amounts of hydrogen are accumulated in the SCO films, both SCO and protonated SCO are insulating, and therefore the protonation and de-protonation have little effect on the electrical properties, resulting in the reduction in ΔR .

We note that the maximum ΔR is found to be correlated with the as-grown resistance. Figure 5c shows the Co concentration dependence of the SFCO channel resistance before the application of $V_{\rm GS}$ (in the asgrown state) and ΔR induced by the application of $V_{\rm GS} \pm 2.0$ and ± 2.5 V. The protonation and de-protonation turn the channels into respectively high- and low-resistance states and, as a result, the films with the lower initial resistance, which probably originates from an electronic structure made from a mixture of Fe³⁺ (3d⁵ and/or 3d⁶L) and Co³⁺ (3d⁶) ions having different electron configurations, can exhibit the enhancement

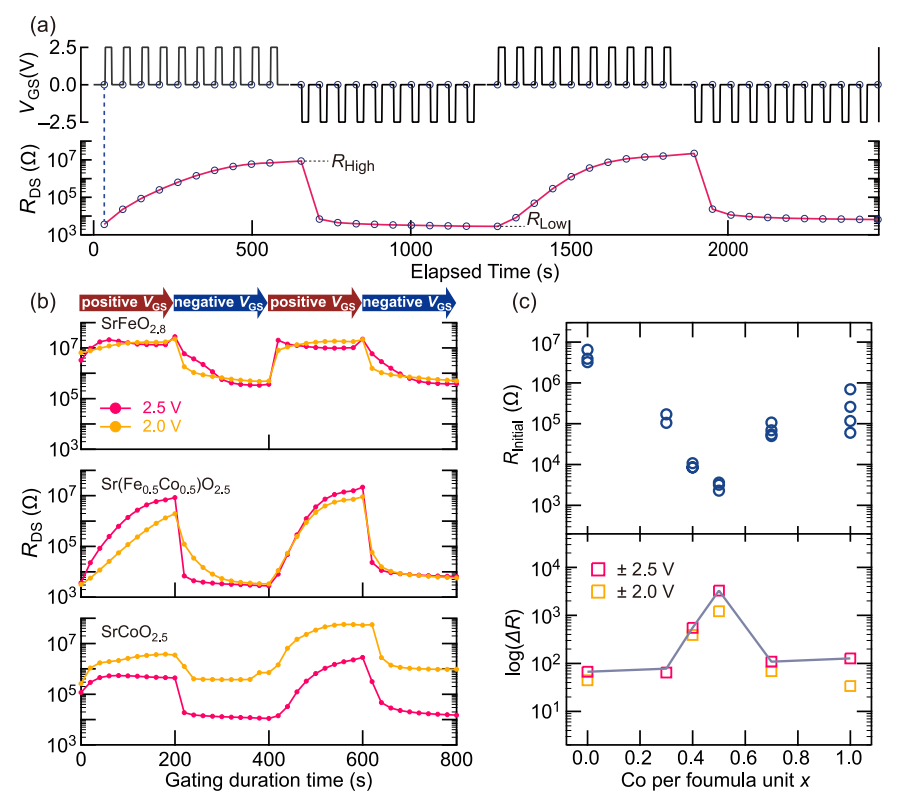


Fig. 5 | **Modulation of electrical resistance of SFCO films by protonation and deprotonation.** a Gate voltage $V_{\rm GS}$ sequence used in our measurements. The illustration at the top shows $V_{\rm GS}$ pulses with durations of 20 s that were repeatedly applied to induce protonation and de-protonation of SFCO films. The total duration of positive and negative $V_{\rm GS}$ pulses for protonation and de-protonation reactions was 200 s. In the interval of $V_{\rm GS}$ pulses, the channel resistance $R_{\rm DS}$ was acquired with a source-drain voltage $V_{\rm SD}$ of 0.1 V and without $V_{\rm GS}$ applied. The bottom graph in the figure shows typical $R_{\rm DS}$ data measured with the $V_{\rm GS}$ sequence. **b** Change in $R_{\rm DS}$

for SrFeO_{2.8}, Sr(Fe_{0.5}Co_{0.5})O_{2.5}, and SrCoO_{2.5} film channels induced by applying $V_{\rm GS} = \pm 2.0$ V and ± 2.5 V. The data were taken for the transistor device with 2-mm-wide and 1 mm-long channels. **c** Co concentration dependence of the SFCO channel resistance before $V_{\rm GS}$ application ($R_{\rm DS}$ in the as-grown state) and the magnitude of the resistance change ΔR induced by application of $V_{\rm G} = \pm 2.0$ and ± 2.5 V. ΔR is defined by the ratio of $R_{\rm DS}$ obtained after applying the last pulse of each positive (or negative) $V_{\rm GS}$ sequence ($\Delta R = R_{\rm High}/R_{\rm Low}$, see Fig. 5a).

in ΔR . We should also point out that, for the SFCO (x = 0.5) films, the initial channel resistance is comparable to those of the low-resistance states induced by de-protonation, highlighting that promoting proton accumulation into and extraction from the SFCO lattices by the oxygen vacancy ordering play a key role in enlarging the resistance change, in stark contrast to previous studies^{11,16} in which resistance changes in brownmillerite-structured oxides and their solid solutions due to proton insertion and extraction have been unexplored.

In summary, we show that room-temperature electrochemical protonation and de-protonation can control the structural and electrical properties of SFCO epitaxial films that were prepared by making a solid solution of the perovskite-structured SrFeO2.8 with disordered oxygen vacancies and the brownmillerite-structured SrCoO25 with ordered oxygen vacancies. As supported by the theoretical calculations, our experimental findings indicate that the oxygen vacancy ordering characteristic of the brownmillerite structure is stabilized by Co substitution for Fe, and it plays a vital role in suppressing oxygen vacancy formation during electrochemical proton injection and in promoting proton insertion and extraction from the SFCO lattices. We also show that for SrFe_{0.5}Co_{0.5}O_{2.5} films, whose electrical resistance is lowest among the SFCO films because of the mixed valence state consisting of Fe³⁺ and Co³⁺, the protonation and de-protonation lead to resistance changes exceeding three orders of magnitude. Our results show that making solid solutions between perovskite- and brownmillerite-structured oxides is useful for controlling oxygen vacancy ordering in oxides and for exploring their functional properties, and they may provide guidelines for controlling material properties through the insertion and extraction of hydrogen and for designing and exploring hydrogen-insertion materials.

Methods

Film growth and X-ray diffraction measurements

 $Sr(Fe_{1-x}Co_x)O_y$ epitaxial thin films were deposited on LSAT (001) single crystal substrates by pulsed laser deposition with a KrF excimer laser (λ = 248 nm). All of the SFCO films were deposited at a substrate temperature of 700 °C and under an oxygen pressure of 100 mTorr, and by pulsing ceramic targets which have nominal cation composition of $Sr(Fe_{1-x}Co_x)O_y$ ($0 \le x \le 1$) with a laser fluence of 1.1J/cm² at a repetition frequency of 4 Hz. X-ray $2\theta/\theta$ diffraction measurements were performed with a lab-source four-circle diffractometer (X'Pert MRD, PANalytical) using Cu K α_1 radiation.

Scanning transmission electron microscopy (STEM) characterization

For the cross-sectional STEM observations, the specimens were thinned down to electron transparency by using focused ion beam (FIB) milling (Helios 5UX, Thermo Fisher Scientific Inc). STEM images were acquired using an aberration-corrected JEM-ARM300F2 (JEOL Ltd) operating at an accelerating voltage of 200 kV. The annular detection angle for HAADF was 54–180 mrad and that for ABF was 12–24 mrad (because the convergent semi-angle of the incident probe was 24 mrad).

Electron energy-loss spectroscopy (EELS) data were acquired at room temperature using an aberration-corrected JEM-ARM200CF instrument (JEOL Ltd) operating at an accelerating voltage of 80 kV. This microscope is also equipped with a cold field–emission gun and an EEL spectrometer (Gatan Quantum). The EEL spectra were collected with an angle of 25 mrad. The energy resolution associated with the EELS analyses was $\sim 1.1\,{\rm eV}$ based on the full width at half-maximum of

the zero-loss peak. The EEL spectra were acquired and processed using the Digital Micrograph software package (Gatan, Inc.). Both low-loss and core-loss spectra were recorded simultaneously using the dual EELS mode with a dispersion of 0.25 eV/channel to allow the concurrent acquisition of Fe $L_{2,3}$ - and Co $L_{2,3}$ -edge spectra. All spectra were obtained in the spectrum imaging mode.

Fabrication of electric field effect transistor structures and electrochemical protonation

To fabricate transistor structures with channels of SFCO films and gate layers of proton-conducting Nafion membranes, we sputtered 30 nmthick Pt drain and source electrodes on the SFCO film at room temperature, and then compressed Nafion membranes (Nafion 115, Sigma Aldrich) with Pt electrodes sputtered on one side on the SFCO films' channel at 110 °C for 15 min. For XRD, ERDA, and XAS measurements, transistor structures with a channel size of ~4 mm \times 5 mm were used. For resistance measurements, transistor structures with a channel size of ~1 mm \times 2 mm were used.

Elastic recoil detection analysis (ERDA)

ERDA was performed at the 1.7 MV tandem accelerator facility of the Quantum Science and Engineering Center, Kyoto University. The ERDA spectra were obtained with 7.5 MeV Si $^{4+}$ beams incident at an angle of \sim 75° to the surface normal and by detecting H atoms recoiled forward from the films at a scattering angle of 30°. The obtained ERDA spectra were simulated and fitted with the SIMNRA 7.03 software 32 .

X-ray absorption spectroscopy (XAS)

Fe and Co K-edge XAS was carried out at beamline BL01B1 in SPring-8 by using a fluorescence method with a 19-element Ge solid state detector. Si (111) double-crystal monochromators were used to obtain the incident X-ray beam. The data analysis was performed using the xTunes software³⁴. O K-edge absorption spectra were measured at beamline BL27SU in SPring-8 by using a partial fluorescence method. The data analysis was performed using Demeter software package³⁵.

Density functional theory calculations

All of our spin-polarized density functional theory calculations were carried out by using the Vienna Ab initio Simulation Package (VASP) package³⁶. The projector augmented wave (PAW) method³⁷ was used to describe the interactions between valance electrons and core ions. The valance electrons were expanded using a plane-wave basis set with an energy cut-off of 550 eV. The Perdew-Burke-Ernzehof (PBE) functional³⁸ within the generalized gradient approximation (GGA) was used to evaluate the exchange-correlation energy with the Hubbard U corrections (PBE + U)³⁹. The effective U values for Fe 3 d and Co 3 d states were 4.00 and 3.32 eV, respectively, which can accurately reproduce the experimental formation enthalpies of iron and cobalt oxides^{40,41}. All atomic positions and lattice parameters were fully optimized until the total force acting on the ions was below 0.02 eV Å⁻¹. The k-mesh with the Monkhorst-Pack scheme and a k-points distance of 0.20 Å⁻¹ was used to sample the Brillouin zone⁴².

The crystal structures of $SrFeO_y$ (y=2.5, 2.75, 2.875, 3.0) were based on the vacancy-ordered phases of $SrFeO_y^{40}$. $SrFeO_y$ with y=2.5 exhibited a brownmillerite structure with a G-type antiferromagnetic state, while $SrFeO_y$ with y=2.75, 2.875, and 3.0 adopt perovskite structures with A-type antiferromagnetic states (y=2.75, 2.875) and a ferromagnetic state (y=3.0). For $SrCoO_y$, we employed similar crystal structures with $SrFeO_y$ for the sake of comparison. The optimized lattice constants are listed in Supplementary Tables S1 and S2.

Data availability

The data that support the plots within this article and other findings of this study are present in the manuscript and the supplementary information and are also available from the corresponding author upon request. The data used to reproduce the results of DFT calculations are available at the Materials Cloud Archive [https://doi.org/10.24435/materialscloud:v0-gn]. Source data are provided in this paper.

References

- Ohta, H. et al. Field-induced water electrolysis switches an oxide semiconductor from an insulator to a metal. Nat. Commun. 1, 118 (2010).
- Li, Z. et al. Reversible manipulation of the magnetic state in SrRuO₃ through electric-field controlled proton evolution. *Nat. Commun.* 11, 184 (2020).
- Tsuchiya, T. et al. In situ tuning of magnetization and magnetoresistance in Fe₃O₄ thin film achieved with all-solid-state redox device. ACS Nano 10, 1655–1661 (2016).
- Jo, M. et al. Gate-induced massive and reversible ohase transition of VO₂ channels using solid-state proton electrolytes. *Adv. Funct. Mater.* 28, 1802003 (2018).
- Shibuya, K. & Sawa, A. Modulation of metal-insulator transition in VO₂ by electrolyte gating-induced protonation. *Adv. Electron. Mater.* 2, 1500131 (2016).
- Yang, J.-T. et al. Artificial synapses emulated by an electrolytegated tungsten-oxide transistor. Adv. Mater. 30, 1801548 (2018).
- Wang, M. et al. Manipulate the electronic and magnetic states in NiCo₂O₄ films through electric-field-induced protonation at elevated temperature. Adv. Mater. 31, 1900458 (2019).
- Wada, T. et al. In situ manipulation of perpendicular magnetic anisotropy in half-metallic NiCo₂O₄ thin film by proton insertion. *Jpn. J. Appl. Phys.* 61, SM1002 (2022).
- Lu, N. et al. Electric-field control of tri-state phase transformation with a selective dual-ion switch. Nature 546, 124–128 (2017).
- Wang, M. et al. Electric-field-controlled phase transformation in WO₃ thin films through hydrogen evolution. Adv. Mater. 29, 1703628 (2017).
- 11. Li, H.-B. et al. Electric field–controlled multistep proton evolution in H₂SrCoO_{2.5} with formation of H–H dimer. *Adv. Sci.* **6**, 1901432 (2019).
- Isoda, Y. et al. Electrochemical control and protonation of the strontium iron oxide SrFeO_y by using proton-conducting electrolyte. Appl. Phys. Lett. 120, 091601 (2022).
- Lefler, B. M., Postiglione, W. M., Leighton, C. & May, S. J. Voltage control of patterned metal/insulator properties in oxide/oxyfluoride lateral perovskite heterostructures via ion gel gating. Adv. Funct. Mater. 32, 2208434 (2022).
- Isoda, Y., Kan, D., Majima, T. & Shimakawa, Y. Orientation-dependent electrochemical reduction and proton evolution in the oxygen-deficient perovskite SrFeO_{2.5+y}. Appl. Phys. Express 16, 015506 (2023).
- Xie, L. et al. Orientation-dependent electrochemical response of LaSrNiO₄ epitaxial films. J. Solid State Electrochem. 28, 4519–4525 (2023).
- 16. Yan, F. et al. Ionic-Liquid-Gating-Induced Hydrogenation in Epitaxial Strontium Ferrite. *Adv. Funct. Mater.* **34**, 2316608 (2024).
- Xie, L. et al. Impact of interfacial proton accumulation on protonation in a brownmillerite oxide. Adv. Funct. Mater. 34, 2410084 (2024).
- 18. Jani, H. et al. Reversible hydrogen control of antiferromagnetic anisotropy in α -Fe₂O₃. *Nat. Commun.* **12**, 1668 (2021).
- Yoon, H. et al. Reversible phase modulation and hydrogen storage in multivalent VO₂ epitaxial thin films. Nat. Mater. 15, 1113–1119 (2016).
- Kamada, T. et al. Ultralong distance hydrogen spillover enabled by valence changes in a metal oxide surface. J. Am. Chem. Soc. 145, 1631–1637 (2023).
- Han, H. et al. Reversal of anomalous hall effect and octahedral tilting in SrRuO₃ thin films via hydrogen spillover. Adv. Mater. 35, 2207246 (2023).

- Shi, J., Zhou, Y. & Ramanathan, S. Colossal resistance switching and band gap modulation in a perovskite nickelate by electron doping. Nat. Commun. 5, 4860 (2014).
- Kim, D., Jeon, Y., MacManus-Driscoll, J. L. & Lee, S. Solid-state catalytic hydrogen sponge effects in BalnO_{2.5} epitaxial flms. Adv. Funct. Mater. 33, 2300819 (2023).
- 24. Miyakawa, M. et al. Fabrication of highly conductive $12CaO \cdot 7Al_2O_3$ thin films encaging hydride ions by proton implantation. *Adv. Mater.* **15**, 1100–1103 (2003).
- 25. Zhou, Z. et al. Effects of dopants and hydrogen on the electrical conductivity of ZnO. *J. Eur. Ceram.* Soc. **24**, 139–146 (2004).
- Lin, J. et al. Hydrogen diffusion and stabilization in single-crystal VO₂ micro/nanobeams by direct atomic hydrogenation. *Nano Lett.* 14, 5445–5451 (2014).
- Chen, Y. et al. Non-catalytic hydrogenation of VO₂ in acid solution. Nat. Commun. 9, 818 (2018).
- Hirai, K. et al. Strain-induced significant increase in metal-insulator transition temperature in oxygen-deficient Fe oxide epitaxial thin films. Sci. Rep. 5, 7894 (2015).
- Katayama, T., Magara, K., Chikamatsu, A. & Hasegawa, T. Anisotropic proton conduction in double-perovskite GdBaCo₂O_{5.5}. Appl. Phys. Lett. 123, 012902 (2023).
- Yamada, H., Kawasaki, M. & Tokura, Y. Epitaxial growth and valence control of strained perovskite SrFeO₃ films. Appl. Phys. Lett. 80, 622–624 (2002).
- 31. Choi, W. S. et al. Strain-induced spin states in atomically ordered cobaltites. *Nano Lett.* **12**, 4966–4970 (2012).
- 32. Mayer, M. SIMNRA User's Guide. Report IPP (1997).
- Ota, T. & Morikawa, Y. Improvement of oxygen storage capacity by charge transfer via oxygen ions in Sr3Fe2–xNixO7.0–δ. Chem. Mater. 36, 8159–8173 (2024).
- Asakura, H. et al. xTunes: A new XAS processing tool for detailed and on-the-fly analysis. Radiat. Phys. Chem. 175, 108270 (2020).
- Ravel, B. & Newville, M. ATHENA, ARTEMIS, HEPHAESTUS: data analysis for X-ray absorption spectroscopy using IFEFFIT. J. Synchrotron Radiat. 12, 537–541 (2005).
- 36. Kresse, G. & Furthmüller, J. Efficient iterative schemes for ab initio total-energy calculations using a plane-wave basis set. *Phys. Rev. B* **54**, 11169–11186 (1996).
- Blöchl, P. E. Projector augmented-wave method. *Phys. Rev. B* 50, 17953–17979 (1994).
- Perdew, J. P., Burke, K. & Ernzerhof, M. Generalized gradient approximation made simple. *Phys. Rev. Lett.* 77, 3865–3868 (1996).
- Dudarev, S. L., Botton, G. A., Savrasov, S. Y., Humphreys, C. J. & Sutton, A. P. Electron-energy-loss spectra and the structural stability of nickel oxide: An LSDA+U study. *Phys. Rev. B* 57, 1505–1509 (1998).
- Alaydrus, M., Hamada, I. & Morikawa, Y. Mechanistic insight into oxygen vacancy migration in SrFeO_{3-δ} from DFT+U simulations. *Phys. Chem. Chem. Phys.* 23, 18628–18639 (2021).
- 41. Jain, A. et al. Formation enthalpies by mixing GGA and GGA + *U* calculations. *Phys. Rev. B* **84**, 045115 (2011).
- 42. Monkhorst, H. J. & Pack, J. D. Special points for Brillouin-zone integrations. *Phys. Rev. B* **13**, 5188–5192 (1976).
- Momma, K. & Izumi, F. VESTA 3 for three-dimensional visualization of crystal, volumetric and morphology data. J. Appl. Cryst. 44, 1272–1276 (2011).

Acknowledgements

This work was partly supported by Grants-in-Aid for Scientific Research (no. 19H05816 (D.K.), 19H05823(Y.S.), 20H05883 (Y.M.), 20H02569 (Y.M.), 21H01810 (D.K.), 22KK0075 (Y.S.), 22H04617 (T.M.), 22H04620 (R.A.), 23H04110 (D.K.), 23H05457 (Y.S.), and 24KJ1371 (Y.I.)) and by grants for the Integrated Research Consortium on Chemical Sciences and the International Collaborative Research Program of the Institute for Chemical Research in Kyoto University from the Ministry of Education, Culture,

Sports, Science, and Technology (MEXT) of Japan. The work was also supported by the Japan Science and Technology Agency (JST) as part of the Advanced International Collaborative Research Program (AdCORP), Grant No. JPMJKB 2304 (Y.S.) and Adopting Sustainable Partnerships for Innovative Research Ecosystem (ASPIRE), Grant No. JPMJAP2312 (D.K.) and JPMJAP2314 (Y.S.), and by JST, the establishment of university fellowships towards the creation of science technology innovation, Grant Number JPMJFS2123(Y.I.). The synchrotron X-ray absorption spectroscopy measurements were performed at the BLO1B1 and BL27SU of SPring-8 with the approval of the Japan Synchrotron Radiation Research Institute (JASRI) (Proposal No. 2023A1631 and 2024A1962). The computations were performed at the Center for Computational Materials Science, Institute for Materials Research, Tohoku University; and at the Institute for Solid State Physics, University of Tokyo. TNP thanks Prof. K. Yamauchi, Dr. T. Ota, and Dr. M. Alaydrus for fruitful discussions.

Author contributions

D.K. conceived the idea and the project plan. Y. I. fabricated samples and performed structural and property characterizations with help from D.K. R.A. carried out cross-sectional STEM observations. Y.I., S.N., and T.M. performed ERDA measurements. Y.I., D.K., S.H., and K.N. performed XAS measurements. T.N.P. and Y.M. carried out theoretical calculations. D.K., Y.M., and Y.S. supervised the project. All authors discussed the experimental and theoretical data, and Y.I., T.N.P., and D.K. co-wrote the manuscript with feedback from all the authors.

Competing interests

The authors declare no competing interests.

Additional information

Supplementary information The online version contains supplementary material available at https://doi.org/10.1038/s41467-024-55517-y.

Correspondence and requests for materials should be addressed to Thanh Ngoc Pham or Daisuke Kan.

Peer review information *Nature Communications* thanks the anonymous reviewer(s) for their contribution to the peer review of this work. A peer review file is available.

Reprints and permissions information is available at http://www.nature.com/reprints

Publisher's note Springer Nature remains neutral with regard to jurisdictional claims in published maps and institutional affiliations.

Open Access This article is licensed under a Creative Commons Attribution-NonCommercial-NoDerivatives 4.0 International License, which permits any non-commercial use, sharing, distribution and reproduction in any medium or format, as long as you give appropriate credit to the original author(s) and the source, provide a link to the Creative Commons licence, and indicate if you modified the licensed material. You do not have permission under this licence to share adapted material derived from this article or parts of it. The images or other third party material in this article are included in the article's Creative Commons licence, unless indicated otherwise in a credit line to the material. If material is not included in the article's Creative Commons licence and your intended use is not permitted by statutory regulation or exceeds the permitted use, you will need to obtain permission directly from the copyright holder. To view a copy of this licence, visit http://creativecommons.org/licenses/by-nc-nd/4.0/.

© The Author(s) 2024